

Two and three impulses phasing strategy with a spacecraft orbiting on an Earth–Moon NRHO

Alberto Fossà^a, Giordana Bucchioni^{a,*}, Emmanuel Blazquez^a, Elisabet Canalias^b,
Stéphanie Lizy-Destrez^a, Régis Bertrand^b, Alain Lamy^b, Jean-Francois Goester^b

^a Department of Aerospace Vehicles Design and Control (DCAS), Institut Supérieur de l'Aéronautique et de l'Espace (ISAE-SUPAERO), 31055 Toulouse, France

^b Centre National d'Études Spatiales (CNES), 18 Avenue Edouard Belin, 31401 Toulouse, France

ARTICLE INFO

Keywords:

Three-Body Problem
Earth–Moon Environment
Python simulator
NRHO
Phasing strategy

ABSTRACT

The increasing interests in Moon exploration have led in recent years to international collaborations between space agencies aimed to assemble and operate the Gateway, an orbiting spaceport located on a Near Rectilinear Halo Orbit (NRHO) about the second libration point of the Earth–Moon system (EML-2). In this context, transfer strategies between the Earth and the spaceport cover a key role for both assembly and resupply missions. The presented work is thus focused on one leg of the transfer: the phasing maneuver. This work is conducted under the hypotheses of the Circular Restricted Three-Body problem (CR3BP) in which the Earth and the Moon are the only bodies that influence the spacecraft motion. The primaries are assumed to have a circular motion around their common barycenter. Under these hypotheses, is demonstrated the existence of periodic orbits, such as the Halo orbit family, that are exploited to design a proposed phasing maneuver. Two strategies are investigated: Halo parking orbit to NRHO two-impulses transfer and direct phasing with manifold exploitation. The first strategy is an optimal two-impulses transfer departing an EML-2 southern Halo and targeting the baseline NRHO. The second strategy considers the chaser already injected on the Gateway's NRHO. Poincaré maps are employed to identify unstable/stable manifolds intersections in search of low-energy phasing trajectories that leave the reference orbit along the unstable branch before re-entering it via the stable one. Three-impulses transfers with similar costs are found patching together these arcs. The two strategies are thus compared to highlight their advantages and disadvantages with the perspective of a real autonomous cargo mission around the Moon to refurbish the orbiting station.

1. Introduction

Since the announcement of the Artemis program in 2017 [1] several studies have been conducted to identify suitable locations for a deep space outpost that would enable sustainable human activities in outer space. Focusing on lunar surface exploration, Whitley and Martinez [2] conduct an extensive trade-off analysis for candidate staging orbits and highlight the favorable properties of Earth–Moon L_2 (EML-2) Near Rectilinear Halo Orbits (NRHOs) regarding Earth and Moon access costs and operational constraints such as Station Keeping (SK) requirements, thermal environment and station to ground communication links. Earth to NRHOs direct transfers in the Circular Restricted Three-Body Problem (CR3BP) are better analyzed by Whitley et al. [3] who find round-trip costs to several members of the NRHO family compatible with Orion-class vehicles. In the same paper, NRHOs to Low Lunar Orbits (LLOs) direct and low-thrust transfers are also studied for crewed and robotic missions to the lunar surface. Finally,

Williams et al. [4] analyze EML-2 NRHOs in the Sun–Earth–Moon (SEM) ephemeris model including the contribution of the Moon's non-uniform gravity potential and perform a multi-year scan to demonstrate frequent access opportunities from Earth exist for the Orion capsule. More recently, an NRHO of the L_2 southern Halo family with an orbit period selected for a 9:2 lunar synodic resonance (i.e. equal to 2/9 the average lunar month or approximately 6.562 days) has been chosen as the Gateway's baseline trajectory for a number of reasons including low SK costs, eclipse avoidance, good coverage over the lunar far side and the Moon's South Pole, almost uninterrupted communication with the Earth and favorable access properties [5].

The presented work is mostly focused on the implementation of a valid simulator of the previously described environment and on the design of a feasible phasing maneuver between an active vehicle that is moving in the proximity of the Moon and a vehicle that is orbiting on the Gateway's NRHO. The authors found a lack in the literature about

* Corresponding author.

E-mail address: Giordana.BUCCHIONI@isae-supaero.fr (G. Bucchioni).

<https://doi.org/10.1016/j.actaastro.2022.06.042>

Received 23 December 2021; Received in revised form 23 May 2022; Accepted 30 June 2022

Available online 6 July 2022

0094-5765/© 2022 IAA. Published by Elsevier Ltd. All rights reserved.

phasing strategies in the presence of third body perturbations but some expertise was taken from previous works focused on orbit to orbit and Earth–Moon transfers.

If operational considerations are key parameters for the candidates' shortlisting, transfer opportunities towards the Earth, the Moon and other CR3BP orbits in the cislunar environment constitute an equivalently important criterion in the final orbit choice. Impulsive transfers between Halo orbits in the Sun–Earth system have been firstly studied by Hiday and Howell [6,7] in the Elliptic Restricted Three-Body Problem (ER3BP) employing Lawden's primer vector theory to optimize the required Δv . These concepts have been recently resumed by Davis et al. [8,9] to compute optimized multi-impulse trajectories between EML-2 Halos in the better known CR3BP model. Exploiting Lawden's findings, Bokelmann and Russell [10] propose an automated procedure to continuously introduce or remove intermediate maneuvers as part of the optimization process and apply the algorithm to solve the endgame problem for interplanetary missions at Europa. Other transfer techniques in the cislunar and translunar environment are addressed by [11,12] which propose an optimal strategy for orbit–orbit strategy, however these approaches require large time of flight that are not suitable for the application of this work. In [13] is investigated the use of Lambert arcs to perform transfers Halo–Halo, highlighting the efficiency of this approach to perform transfers in the Earth–Moon framework, nevertheless no mention of phasing maneuver is done in this work. Instead, phasing trajectories from the Gateway's nominal NRHO to several Low Lunar Orbits are analyzed by Bucchioni and Innocenti [14] using a differential correction procedure fed with the Lambert problem or the Hohmann transfer's solution in the R2BP as suitable initial guesses. Finally, Davis et al. [15] employ two-body parameters to design bridging trajectories between unstable/stable manifolds of the departure/arrival orbits and minimize the resulting Δv for Halo to Halo transfers in both the Sun–Earth and Earth–Moon CR3BP systems. These works suggest that gradient information coded in the State Transition Matrix (STM) of the propagated spacecraft state can be exploited to formulate robust iterative schemes for the optimization of direct and low-energy transfers in multi-body dynamical regimes. The same concepts are thus employed in this paper to derive a Δv minimization scheme for phasing with spacecrafts orbiting on EML-2 NRHOs.

The scope of this work is in fact to provide two different approaches to allow a chaser vehicle, once arrived in the proximity of the Moon, to recover the phase difference and start the rendezvous maneuver with a passive target orbiting a specific NRHO. In other words, the phasing maneuver is defined as the connection between the end of the Earth–Moon transfer and the beginning of the proximity operations. The target vehicle can in fact be located at any point along its orbit at the time the chaser arrives in the Moon's proximity. Nevertheless, the last must be capable of approaching the target vehicle for a wide range of possible relative configurations. Two different ways of performing this operation are thus proposed: the first one exploits the natural dynamics of parking orbits to recover the necessary orbital phase while the second uses the invariant manifolds and their dynamics to achieve the same goal.

The paper is organized as follows: first, the working scenario and the simulation environment are clearly stated. Afterwards, the phasing design strategies are explained. The results are then presented and commented, to conclude with some comments.

2. Working scenario

2.1. Reference systems and equations of motion

Preliminary mission design in the cislunar realm is often carried out in the Circular Restricted Three-Body Problem (CR3BP) since it provides full insight into the dynamical behavior of a spacecraft traveling in the Earth–Moon region while avoiding much of the computational effort required by higher fidelity ephemeris models. This model admits

five equilibrium solutions known as libration or Lagrange points, which constitute the origin of several families of periodic orbits that evolve both in-plane and out-of-plane from these locations with increasing amplitude. Throughout this work, periodic solutions in the CR3BP are computed employing differential correction techniques and transitioned into higher fidelity force models to exploit their suitability as staging orbits for the future Lunar Gateway. As a consequence, the Equations of Motion (EOMs) governing the spacecraft dynamics in the CR3BP are presented in the following sections to analyze the dynamical structures that characterize the regions of interest.

The EOMs in the CR3BP are conveniently formulated in a rotating reference frame such that the positions of the primaries remain fixed. Also known as synodic frame, the reference has its origin at the primaries' barycenter and the x axis along the $P_1 - P_2$ direction pointing towards the smaller body with P_1, P_2 positions of m_1, m_2 respectively, where m_1 and m_2 are the masses of the two primaries. The z axis is aligned with the primaries' angular momentum vector while the y axis completes the right-handed orthogonal coordinate system.

From the above definition and Eq. (1) the positions of m_1 and m_2 are retrieved as $P_1 = (-\mu, 0, 0)$ and $P_2 = (1 - \mu, 0, 0)$ respectively, note that according with the literature [16] all the quantities are normalized, therefore the results are retrieved in normalized units and denormalized just to increase their readability. An inertial frame is also defined such that the z axes coincide at all times while the x and y axes overlap at $t = 0$ as depicted in Fig. 1

$$\mu = \frac{m_2}{m_1 + m_2} \quad (1)$$

The gravitational potential energy experienced by the third particle due to the gravitational pull of m_1 and m_2 is then expressed in the rotating frame defined above as in equation Eq. (2), according to the definition given in [16]

$$U(x, y, z) = -\frac{1 - \mu}{r_1} - \frac{\mu}{r_2} - \frac{1}{2}\mu(1 - \mu) \quad (2)$$

where the first and second terms are the contributions of the two primary bodies and the last an arbitrary constant that simplifies the subsequent derivation of the corresponding EOMs. Finally, r_1 and r_2 are the distances between the particle and the two primaries computed as

$$\begin{aligned} r_1 &= \sqrt{(x + \mu)^2 + y^2 + z^2} \\ r_2 &= \sqrt{(x - 1 + \mu)^2 + y^2 + z^2} \end{aligned} \quad (3)$$

The second-order EOMs in the synodic frame and normalized units are then given by

$$\begin{aligned} \ddot{x} - 2\dot{y} &= -\frac{\partial \bar{U}}{\partial x} \\ \ddot{y} + 2\dot{x} &= -\frac{\partial \bar{U}}{\partial y} \\ \ddot{z} &= -\frac{\partial \bar{U}}{\partial z} \end{aligned} \quad (4)$$

with \bar{U} augmented or effective potential energy defined as

$$\begin{aligned} \bar{U} &= -\frac{1}{2}(x^2 + y^2) + U(x, y, z) \\ &= -\frac{1}{2}(x^2 + y^2) - \frac{1 - \mu}{r_1} - \frac{\mu}{r_2} - \frac{1}{2}\mu(1 - \mu) \\ &= -\frac{1}{2}((1 - \mu)r_1^2 + \mu r_2^2) - \frac{1 - \mu}{r_1} - \frac{\mu}{r_2} \end{aligned} \quad (5)$$

In the context of this work the two primaries are the Earth (m_1) and the Moon (m_2).

The literature shows that numerical techniques need to be employed both to integrate Eq. (4) and to compute equilibrium, periodic and quasi-periodic solutions of the former EOMs [16]. Periodic solutions are then cataloged based on their properties and shape in what are known as periodic orbit families. Other non-periodic solution to the system

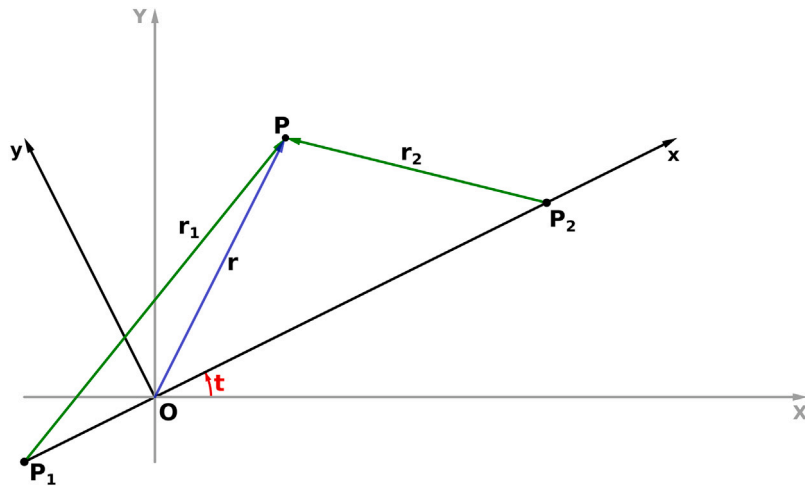


Fig. 1. Synodic and inertial reference frames. (For interpretation of the references to color in this figure legend, the reader is referred to the web version of this article.)

ODEs exist, such as invariant manifolds which are open trajectories that asymptotically converge or diverge to/from periodic orbits.

For a given orbit, an insight on the existence and direction of associated invariant manifolds is obtained from the eigenvalues and eigenvectors of the Monodromy matrix M defined as

$$\delta \mathbf{x}(T, \mathbf{x}_0) = \Phi(T, \mathbf{x}_0) \delta \mathbf{x}_0 \implies M := \Phi(T) = \frac{\partial \mathbf{x}(T)}{\partial \mathbf{x}_0} \quad (6)$$

where \mathbf{x}_0 is the equilibrium point around which the dynamics is linearized, $\delta \mathbf{x}_0$ the perturbation around the equilibrium point, $\Phi(t, \mathbf{x}_0)$ the STM, and T is the orbital period. The invariant manifolds are generated perturbing the orbital dynamics in the direction associated with the unitary eigenvalues of the Monodromy matrix and they globally look as tubes that converge or diverge towards or from the orbit [17].

The definition of the Jacobi constant C_{jac} is also provided to show the importance of the presented results. C_{jac} is the only integral of motion admitted by Eq. (4) and a measure of the energy of the orbit. It is defined as

$$C_{jac}(x, y, z, \dot{x}, \dot{y}, \dot{z}) = -(\dot{x}^2 + \dot{y}^2 + \dot{z}^2) - 2\bar{U} \quad (7)$$

Stability indexes are another key quantity to measure the stability characteristics of the involved orbits. The stability indexes are denoted as s_1 and s_2 and they are defined as in Eq. (8)

$$\begin{aligned} s_1 &= 0.5(\lambda_1 + \lambda_2) \\ s_2 &= 0.5(\lambda_5 + \lambda_6) \end{aligned} \quad (8)$$

where λ_i for $i = 1, 2, 5, 6$ are the non-trivial eigenvalues of the Monodromy matrix such that $\lambda_1 = 1/\lambda_2$ and $\lambda_5 = \bar{\lambda}_6$. These values are associated to the stable/unstable manifolds and to the neutral mode of the orbit. The remaining ones $\lambda_3 = \lambda_4 = 1$ are associated to the periodical nature of the Halo orbits. An idea of the physical meaning of the stability indexes can be give if it is considered that for a diverging path, a larger value of the stability index corresponds to a faster departure from the reference. See [18] for more details.

2.2. Simulation environment: SEMPY

Numerical methods employed in this work have been implemented as part of SEMPY (Sun–Earth–Moon in Python), a research tool for mission design in non-Keplerian environments coded in Python. The software package is developed and maintained by the SaCLab (Space Advanced Concepts Laboratory) team at ISAE-SUPAERO [19].

It provides powerful astrodynamics tools focused on non-Keplerian space mechanics with a user-friendly interface and is meant for both

research and education purposes. Contributions to the library are included complying with the SEMPY development workflow which includes static code analysis, unit tests, integration tests, and rigorous documentation of each newly implemented feature. Moreover, state-of-the-art astrodynamics tools and libraries such as GMAT [20], CelestLab [21], Orekit, [22] and SEMAT [23,24] are used to validate the implemented algorithms when possible. SEMPY is based on Python 3.8 and takes advantage of several packages for scientific computing available in the programming language ecosystem.

2.3. Working framework: Halo family and target orbit description

The existence of periodic or quasi-periodic orbits about the collinear libration points of any CR3BP system is known since the mid-twentieth century and to date, a complete description and computation of those solutions have been obtained [16]. In particular, for the Earth–Moon system, L_2 Halo orbits are three-dimensional periodic solutions that bifurcate from planar Lyapunov orbits near the L_2 libration point and evolve out of the plane while approaching the Moon [2].

Given the inherent symmetry of the EOMs concerning the xy plane, both northern and southern Halo families exist which differ only in the opposite values of the z components of the state vector \mathbf{x} at any point along the path. Northern Halos have periselene (the closest point of the orbit to m_2) locations below the xy plane ($z_p < 0$) while spacecraft injected in these orbits spend most of the time above it. The opposite is true for southern ones. In this work, Halo families are computed numerically with a continuation scheme based on the differential correction procedures described in Pavlak [25]. A first solution close to L_2 (vertical extension $A_z \approx 10$ km) is obtained analytically using the third-order approximation derived by Richardson [26] and then corrected applying a differential correction procedure.

Earth–Moon L_2 NRHOs are a subset of EML-2 Halos characterized by bounded stability and an elongated shape almost perpendicular to the xy plane in the canonical rotating frame previously defined [18]. The current baseline orbit for the Gateway is a 9:2 resonant southern NRHO which falls within this range as highlighted in Fig. 2 in green. It has been selected since it provides good accessibility properties from the Earth and the Moon, almost complete Earth coverage, a stable thermal environment, and favorable eclipsing properties [2,18]. Its characteristics are summarized in Table 1 while Fig. 2 depicts the EML-2 southern Halo family in blue with the NRHO subset highlighted in green and the Gateway orbit plotted in black.

Given similar properties are shared across the family, Halo members closer to the L_2 libration point are then investigated as possible parking orbits for phasing maneuvers.

Table 1

Characteristics for the 9:2 synodic resonant EML-2 southern NRHO (Gateway baseline orbit).

Vertical extension	A_z	69958.505 km
Periselene radius	r_p	3225.211 km
Aposelene radius	r_a	71 170.507 km
Period	T_{NRHO}	6.562 days
Jacobi constant	C_{jac}	3.059
Stability indexes	s_1, s_2	-1.318, 0.684

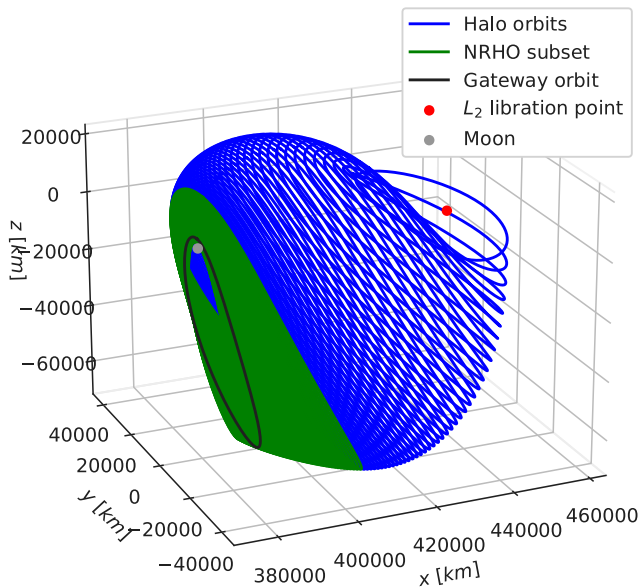


Fig. 2. EML-2 southern Halo orbits family and NRHO subset ($1832.63 \text{ km} < r_p < 17390.67 \text{ km}$, $5.98 \text{ days} < T < 10.36 \text{ days}$) in synodic frame. (For interpretation of the references to color in this figure legend, the reader is referred to the web version of this article.)

For non-keplerian orbits, formal definitions of phase and phase difference do not exist. In the attempt of finding a parallelism between two-body and three-body orbits, for Halo members the phase is defined as the fraction of orbit period elapsed since the last periselene passage given by

$$\theta = \frac{t - t_p}{T} \quad \theta \in [0, 1] \quad (9)$$

with t current time, t_p time at last periselene passage and T orbit period. Eq. (9) is used to describe two-impulses transfer while an alternative definition expressed in units of time is more suitable for the three-impulses scenario

$$\Delta t = \theta T \quad \Delta t \in [0, T] \quad (10)$$

3. Phasing maneuver design: Optimized two-impulses and low energy three impulses

As anticipated in the introduction, two different phasing strategies to recover some orbital phase are presented in this section. The optimized two-impulse approach uses a parking orbit to decouple the Earth–Moon transfer phase and the rendezvous operations, moreover selects the best orbit, among the Halo family, to maximize the exploitation of the natural capability of the parking orbit of recovering some phase. The choice of the parking orbit among the Halo family is motivated by the fact that the target orbit belongs to the same family, therefore they have similar properties in terms of shape and energy. The three-impulses approach, instead, avoids the use of a parking orbit. The chaser vehicle enters directly on the target NRHO and exploits the natural dynamics of the invariant manifolds to recover the phase

mismatch. The two strategies are meant to address the problem of phasing in different scenarios, and thus their domains of applicability do not intersect. The technical details are provided in the followings.

3.1. Optimized two-impulses phasing

The optimized two-impulses strategy formalized in this paper is composed of two steps: the selection of the parking orbit and the assessment of the performances of the selected parking orbits in terms of waiting time, time of flight, energy consumption, and phasing capabilities.

The following describes how the impulsive maneuver is computed and optimized, and how this optimization procedure is used for the selection of a parking orbit among the Halo family. The procedure for the performance assessment is finally detailed.

3.1.1. Lambert transfer

Spacecraft mission design usually requires the determination of transfer trajectories that link two given orbits or points in space. If the departure position, arrival position, and Time of Flight (TOF) for these transfers are imposed, the problem is known as the Lambert problem and coincides with the following Two-Point Boundary Value Problem (TPBVP)

$$\begin{cases} \dot{\mathbf{x}}(t) = \mathbf{f}(t, \mathbf{x}(t), \lambda) \\ \mathbf{r}(t_d) = \mathbf{r}_d \\ \mathbf{r}(t_a) = \mathbf{r}_a \end{cases} \quad (11)$$

with $\mathbf{f}(t, \mathbf{x}(t), \lambda)$ first-order ODEs governing the spacecraft motion in the selected dynamical regime, $\mathbf{x}(t) = [\mathbf{r}(t) \ \mathbf{v}(t)]^T$ spacecraft state and $\Delta t = t_d - t_a$ specified TOF. The subscripts d and a refer to departure and arrival respectively. Analytical solutions to Eq. (11) are known to exist in the R2BP model and several algorithms have been proposed to solve the underlying equations via simple root-finding algorithms. However, no closed-form solution exists in more complex dynamical regimes.

Numerical techniques based on the multiple shooting procedures [25] are developed in this work to compute fixed-time transfers between specified orbits or spacecraft positions in the CR3BP model. The implemented algorithm consists of the following steps:

1. Specification of the positions of the endpoints $\mathbf{r}_d, \mathbf{r}_a$ and transfer time TOF.
2. Selection of the number of patch points on which differential correction is applied.
3. Computation of a suitable initial guess with the R2BP Lambert solution.
4. Correction of the patch points states.
5. Computation of the impulsive maneuvers required to perform the transfer.

3.1.2. Optimization algorithm

If the standard formulation of the Lambert problem assumes fixed endpoints positions and Time of Flight (TOF), for orbit to orbit transfers it is more convenient to relax these assumptions and determine the departure location within the departure orbit θ_d , arrival location within the arrival orbit θ_a (Eq. (9)) and TOF that lead to the lowest cost transfer in terms of the total required Δv . Denoting with $\mathbf{X} = [TOF, \theta_d, \theta_a]^T$ the design variables vector, the corresponding optimization problem is then stated as follows.

Minimize

$$J(\mathbf{X}) = \|\Delta \mathbf{v}_d\| + \|\Delta \mathbf{v}_a\| = \|\mathbf{v}(t=0) - \mathbf{v}_d\| + \|\mathbf{v}_a - \mathbf{v}(t=TOF)\| \quad (12)$$

Subject to

$$\begin{aligned} \dot{\mathbf{x}}(t) &= \mathbf{f}(\mathbf{x}(t), \mu) \\ \mathbf{r}(0) &= \mathbf{r}_d \\ \mathbf{r}(TOF) &= \mathbf{r}_a \end{aligned} \quad (13)$$

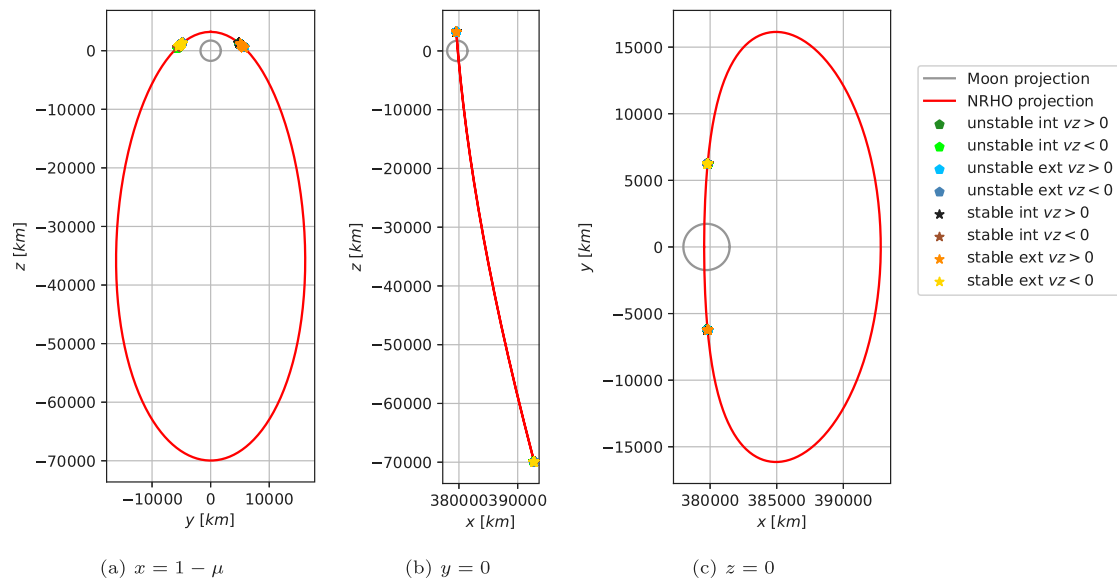


Fig. 3. Poincaré maps for target NRHO stable and unstable manifold branches. (For interpretation of the references to color in this figure legend, the reader is referred to the web version of this article.)

with $f(\mathbf{x}(t), \mu)$ first-order EOMs in the CR3BP, $\mathbf{x}(t) = [\mathbf{r}(t) \ \mathbf{v}(t)]^T$ state vector along the transfer and $\mathbf{x}_d = [\mathbf{r}_d \ \mathbf{v}_d]^T$, $\mathbf{x}_a = [\mathbf{r}_a \ \mathbf{v}_a]^T$ state vectors on the departure and arrival orbits prior to $\Delta \mathbf{v}_d$ and after $\Delta \mathbf{v}_a$ respectively.

3.1.3. Optimized two-impulses transfer

The analysis is comprised of the following steps.

1. Definition of the target NRHO from continuation procedure [25].
2. Definition of 40 departure Halos with equally spaced periods $T_d \in [T_a, 14.80 \text{ days}]$ with T_a Gateway orbit's one ($T_a = T_{NRHO}$).
3. Definition of 40 departure and arrival positions θ_d, θ_a uniformly spaced in time with $\theta_d, \theta_a \in [0, 1[$ given by Eq. (9).
4. Computation of direct transfers for all possible combinations of T_d, θ_d, θ_a detailed above and both zero ($\Delta\theta < 1$) or one ($\Delta\theta > 1$) complete revolutions about the Moon.
5. Selection of the lowest-cost transfer between 0 or 1 revolutions for every combination of endpoint orbits (T_d) and positions (θ_d, θ_a).
6. TOF optimization $\forall T_d, \theta_d, \theta_a$ with θ_d, θ_a fixed and free variables vector \mathbf{X} reduced to $\mathbf{X} = [TOF]^T$.
7. Selection of the departure and arrival positions θ_d, θ_a that lead to the lowest-cost transfer for every value of T_d and construction of an initial guess \mathbf{X}_0 for the subsequent step.
8. Concurrent optimization of θ_d, θ_a and TOF for each departure Halo (or T_d value) using algorithm described above with $\mathbf{X} = [TOF, \theta_d, \theta_a]^T$ and \mathbf{X}_0 obtained before.

This procedure leads to the selection of a specific parking orbit. Afterward, the performances of the selected orbit are assessed through the following procedure.

1. Definition of the departure Halo selected as the output of the previous analysis.
2. Definition of 40 positions $\theta_{a,0}$ for the station at the time the chaser is assumed to be at the Halo orbit periselenes ($\theta_{d,0} = 0$).
3. Definition of a wait time (WT) grid $WT = 0 : \Delta_{WT} : T_{syn}$ with $\Delta_{WT} = 30 \text{ min}$ and T_{syn} computed as

$$T_{syn} = \frac{T_d \cdot T_a}{|T_d - T_a|} \quad (14)$$

with T_d, T_a departure and arrival orbit periods respectively.

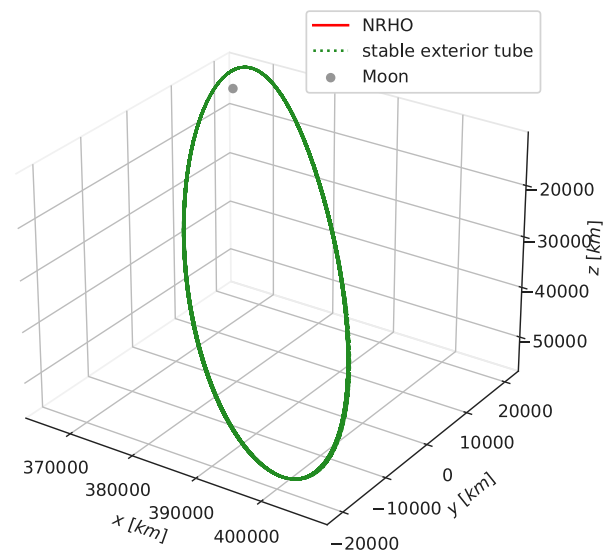


Fig. 4. Stable exterior manifold for the target nominal NRHO. (For interpretation of the references to color in this figure legend, the reader is referred to the web version of this article.)

4. Definition of a TOF grid $TOF = 0 : \Delta_{TOF} : T_d$ with $\Delta_{TOF} = 30 \text{ min}$.
5. Computation of θ_d, θ_a from $\theta_{d,0}, \theta_{a,0}$ and WT, TOF via the following equation

$$\begin{cases} \theta_d = \left(\theta_{d,0} + \frac{WT}{T_d} \right) \bmod 1 \\ \theta_a = \left(\theta_{a,0} + \frac{WT + TOF}{T_a} \right) \bmod 1 \end{cases} \quad (15)$$

with T_d, T_a departure and arrival orbit periods given above.

6. Solution of the standard Lambert problem with fixed endpoint positions and TOF for all initial configurations.
7. Analysis of the WT, TOF and Δv variations with respect to $\theta_{a,0}$.

At this point, the performances are verified.

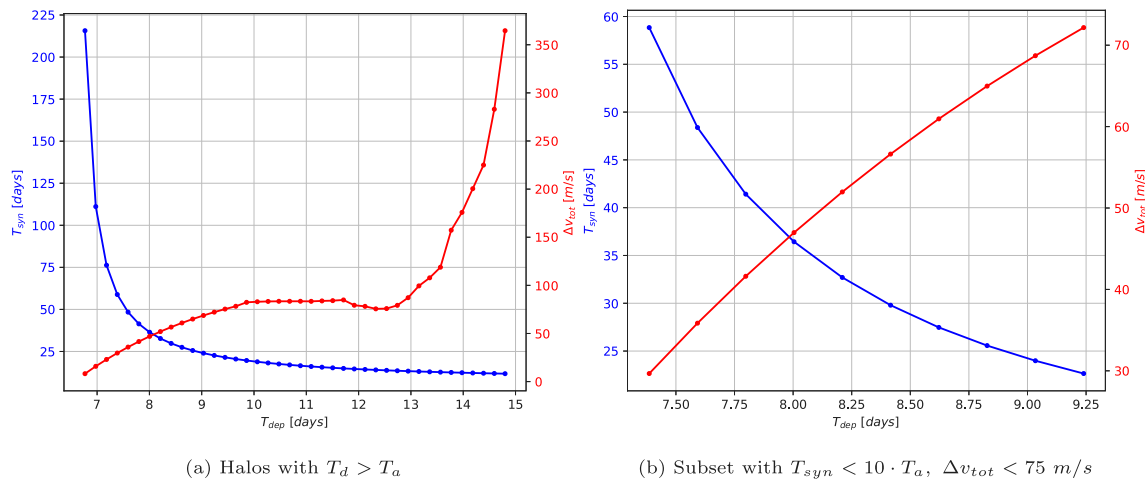


Fig. 5. Optimal Δv and Halo-NRHO synodic period w.r.t. Halo orbit period for direct two-impulse transfers between EML-2 southern Halo members. (For interpretation of the references to color in this figure legend, the reader is referred to the web version of this article.)

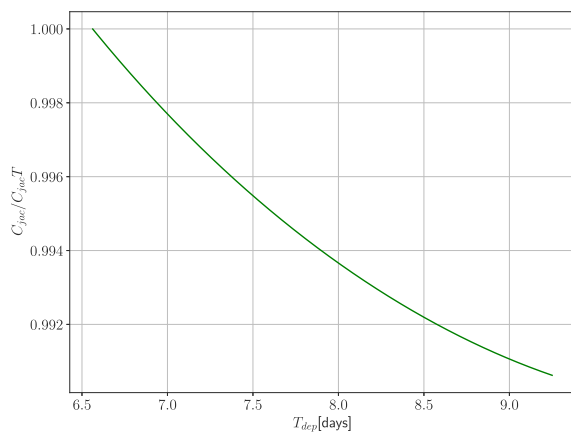


Fig. 6. Ratio between the Jacobi constant of all the orbits with $T_d > T_a$ and $T_{syn} < 10 \cdot T_a$. (For interpretation of the references to color in this figure legend, the reader is referred to the web version of this article.)

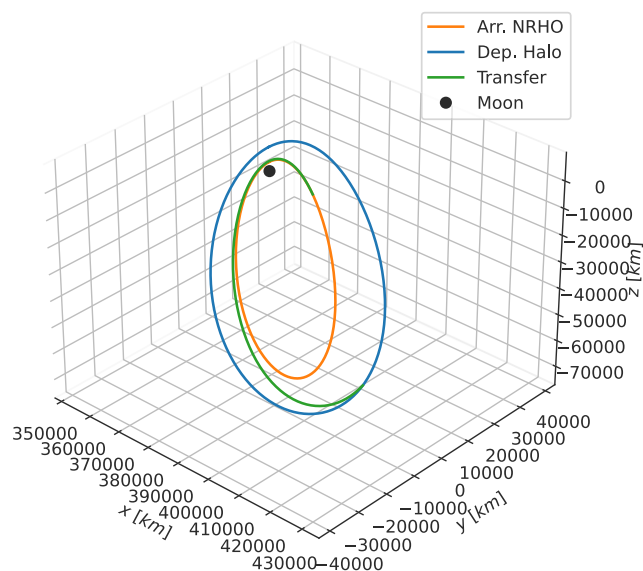


Fig. 7. Two-impulse transfer from EML-2 Halo with $T_d = 8.21$ days $R_p = 8626.920$ km to target nominal NRHO with $T_a = 6.56$ days and $R_p = 3225.211$ km in the Earth-Moon synodic frame. (For interpretation of the references to color in this figure legend, the reader is referred to the web version of this article.)

3.2. Low energy three impulses phasing

In this second strategy, the natural structures of the NRHO such as the manifolds [16] are exploited to recover the phase difference. This strategy is suitable for a chaser vehicle already orbiting in proximity of the target station for which a finer phasing is required.

Given the existence of stable and unstable invariant manifolds associated with the designed NRHO, low-energy transfers might exist that connect asymptotically diverging paths with the corresponding converging ones. For given departure and arrival locations, if the transfer time along these trajectories is significantly different for the TOF along the nominal orbit, the former might be seen as a low-energy phasing option to move the chaser vehicle closer to the station.

Longer TOFs are required for spacecraft initially ahead of the Gateway while shorter ones are needed for vehicles initially behind the station. Since continuity in the spacecraft position vector is required along with the transfer, intersections between unstable and stable manifolds are sought to determine feasible transfer paths. Moreover, continuity in the velocity vector is separately enforced along the diverging and converging branches while a mismatch at manifolds intersection indicates an impulsive maneuver is required to perform the transfer. At the same time, no deterministic maneuvers are needed to leave the initial orbit along the unstable manifold branch and to re-inject in the nominal path from the stable one. However, an infinite amount of time is required to depart from periodic orbits in the CR3BP and small impulsive maneuvers are then introduced to perturb the spacecraft state and limit the total transfer time.

The design of this strategy is performed through the following steps.

1. The manifolds of the target NRHO are studied for different Poincare maps. In particular, the intersection between stable/unstable, internal/external manifolds is studied.
2. The Poincare map that allows the largest phase recovery is selected for transfer design.
3. The Δv that is required to escape the NRHO to enter the selected unstable manifold, to connect the stable and the unstable manifold, and to enter the NRHO again is computed and the TOF gain assessed.
4. A sensitivity analysis is performed to study the influence of the selected manifold branch on the performance of the phasing.

3.2.1. Manifold study

Intersections between unstable and stable manifold tubes are localized looking at the Poincare maps obtained piercing different Poincare sections with a great number of discrete manifold branches. Three sections are considered in this work (See Fig. 3)

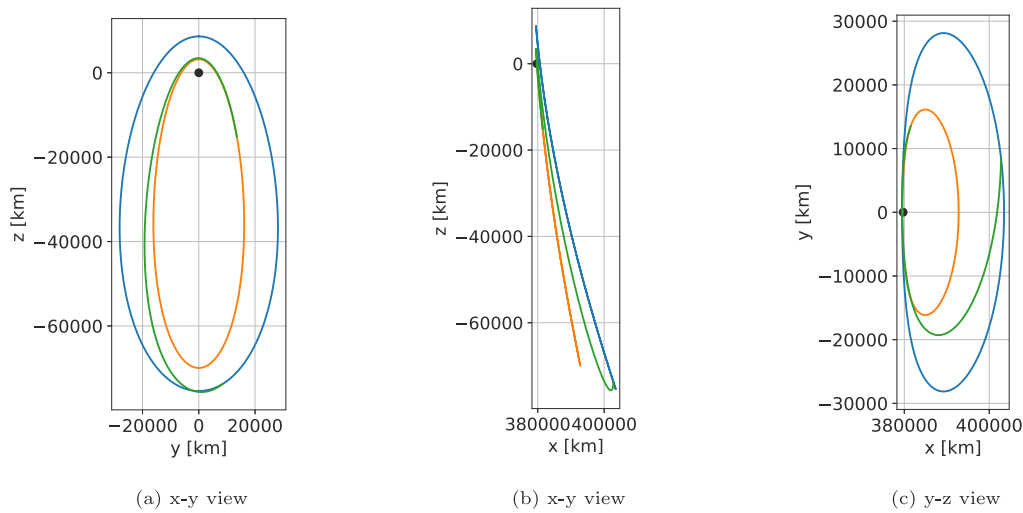


Fig. 8. Two-impulse transfer from EML-2 Halo with $T_d = 8.21$ days $R_p = 8626.920$ km to target nominal NRHO with $T_a = 6.56$ days and $R_p = 3225.211$ km in the Earth–Moon synodic frame — plane views. (For interpretation of the references to color in this figure legend, the reader is referred to the web version of this article.)

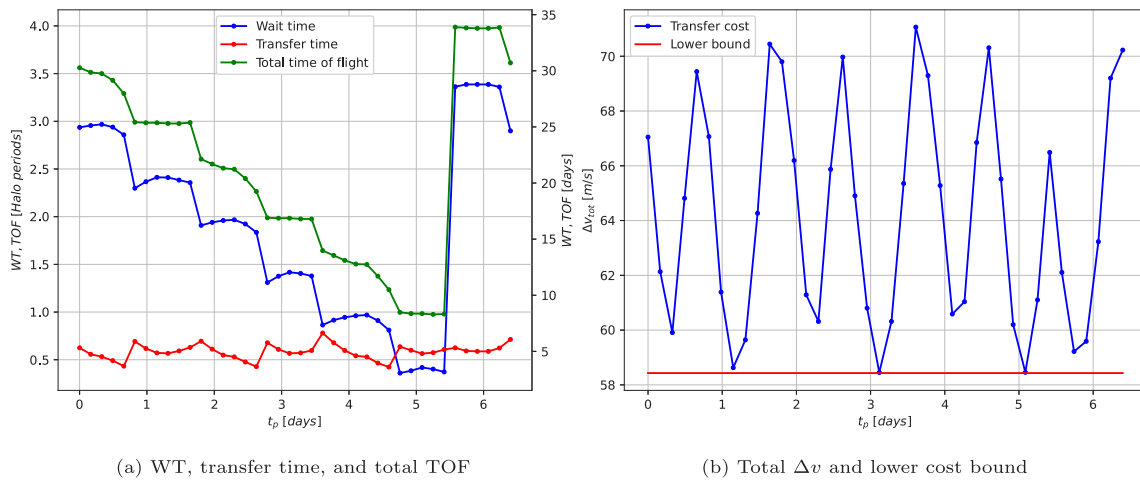


Fig. 9. Transfer times and total Δv w.r.t. target's time since periselene passage for direct two-impulse RDV maneuvers from EML-2 southern Halo with $T = 8.5$ days to target NRHO. (For interpretation of the references to color in this figure legend, the reader is referred to the web version of this article.)

1. $x = 1 - \mu$: yz plane perpendicular to $P_1 - P_2$ passing through the center of the Moon.
2. $y = 0$: xz plane defined by $P_1 - P_2$ and the primaries' angular momentum vector.
3. $z = 0$: xy plane in which the primaries' motion takes place.

To populate the above-defined sections, each manifold tube is discretized into 400 branches departing the nominal NRHO from an equal number of evenly spaced positions $\theta_i \in [0, 1[$.

For each θ_i the initial states along the four manifold branches (unstable/stable - U/S - and interior/exterior - I/E) are computed [16] and propagated forward or backward in time for two target orbit periods (about 13.12 days) so that the defined sections are crossed in both positive ($v_\perp > 0$) and negative ($v_\perp < 0$) directions (see Fig. 4 for an example of exterior stable tube propagation).

For each manifold tube, crossing direction and θ_i , the first plane crossing \mathbf{x}_c characterized by a TOF since the initial perturbation $|t_c| > T_{NRHO}/2$ is then recorded and displayed on its respective section to identify possible intersections. Note that all the quantities with the subscript c are referred to the crossing state.

Propagated for $t_{prop} = 2 \cdot T_{NRHO}$, the Stable Exterior (SE) manifold (dark green curves) represented in this figure is in fact indistinguishable from the baseline NRHO (red curve) since the perturbed paths lie

in very close proximity of the periodic orbit for the considered time span. Longer propagation times would allow the spacecraft to reach farther regions and possibly increase the number of available phasing trajectories but they are discarded due to impractical TOF.

For each cluster and tube and each Poincaré map, recorded intersections form a straight line of points corresponding to different positions along the orbit in which the perturbation is firstly applied. A small region where the four segments overlap is also identified thus indicating possible bridges between diverging and converging paths.

States components $\mathbf{x}_c^{U\pm} = [\mathbf{r}_c^{U\pm} \ \mathbf{v}_c^{U\pm}]^T$ and $\mathbf{x}_c^{S\pm} = [\mathbf{r}_c^{S\pm} \ \mathbf{v}_c^{S\pm}]^T$ extracted from the above depicted maps are then used to compute the position difference $\Delta \mathbf{r}$ between all possible combinations of unstable and stable branches on the three selected surfaces to identify possible intersections. A threshold $\Delta r = 200$ m is chosen in this work to discriminate between intersecting and non-intersecting trajectories. The relatively large value of Δr is justified by the different assumptions introduced with the underlying force model and manifold computation strategy which require the trajectory to be adjusted in a higher fidelity model to obtain truly continuous paths.

Firstly, position differences $\Delta \mathbf{r}$ are given by

$$\Delta \mathbf{r} = \|\Delta \mathbf{r}\|_2 = \|\mathbf{r}_c^{U\pm} - \mathbf{r}_c^{S\pm}\|_2 \quad (16)$$

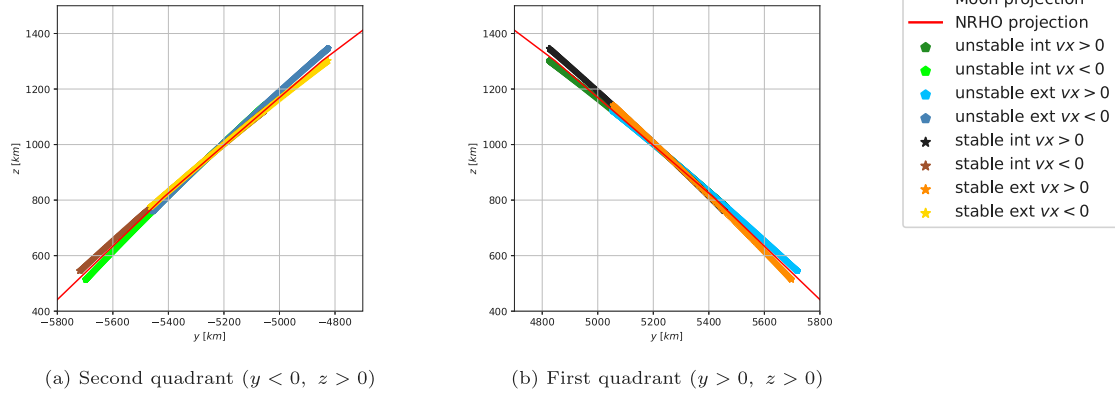


Fig. 10. Poincaré map at $x = 1 - \mu$ for target NRHO stable and unstable manifolds. (For interpretation of the references to color in this figure legend, the reader is referred to the web version of this article.)

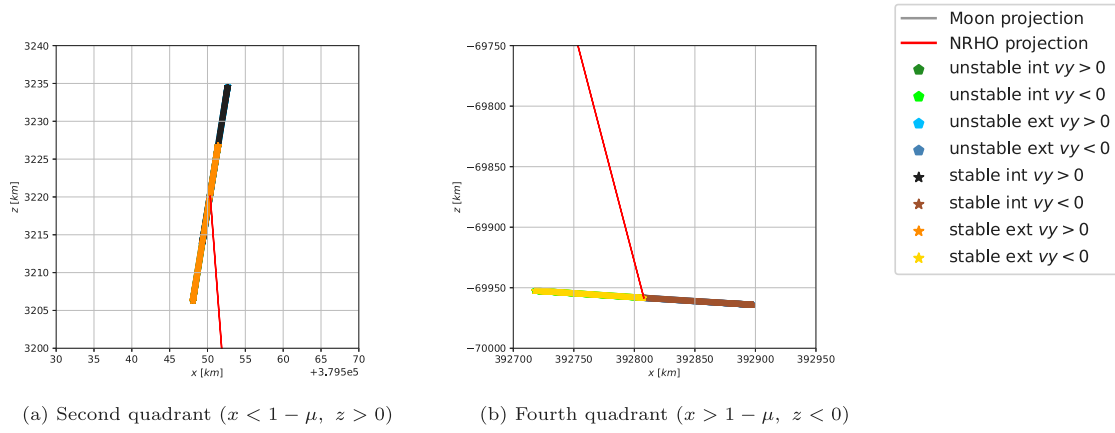


Fig. 11. Poincaré map at $y = 0$ for target NRHO stable and unstable manifolds. (For interpretation of the references to color in this figure legend, the reader is referred to the web version of this article.)

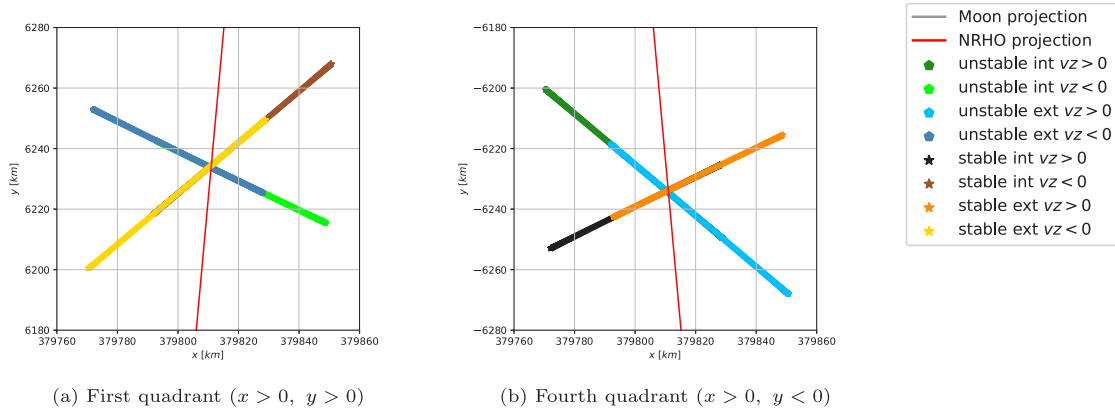


Fig. 12. Poincaré map at $z = 0$ for target NRHO stable and unstable manifolds. (For interpretation of the references to color in this figure legend, the reader is referred to the web version of this article.)

Secondly, total transfer time t_{man} and required Δv are computed as

$$t_{man} = |t_c^{U\pm} - t_0^{U\pm}| + |t_c^{S\pm} - t_0^{S\pm}| = t_c^{U\pm} + |t_c^{S\pm}| \quad (17)$$

$$\Delta v = \|\Delta \mathbf{v}\|_2 = \|\mathbf{v}_c^{U\pm} - \mathbf{v}_c^{S\pm}\|_2 \quad (18)$$

since $t_0^{U\pm} = t_0^{S\pm} = 0$ and $t_c^{S\pm} < 0$. Note that all three components of $\Delta \mathbf{v}$ are generally not null given that each branch intersects the corresponding plane with different incidence angles.

Once t_{man} is known, the corresponding TOF difference resulting from flying along the perturbed path rather than the nominal NRHO is computed as

$$\begin{aligned} \Delta t &= \min_{n \in \mathbb{N}} |t_{man} - T_a \cdot (\Delta \theta + n)| \\ &= \min_{n \in \mathbb{N}} |t_{man} - T_a \cdot (\theta_0^{U\pm} - \theta_0^{S\pm} + n)| \end{aligned} \quad (19)$$

where the non-negative integer n corresponds to the number of complete revolutions along the nominal path which leads to the lowest value of Δt . Taking the minimum over n allows to discard artificial

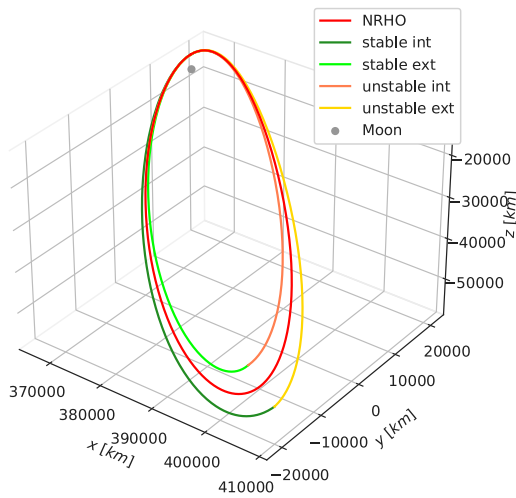


Fig. 13. Three-impulse phasing trajectories with $\Delta v_0 = 8$ m/s and highest TOF difference. UI to SE transfer in orange/light green, UE to SI in yellow/dark green. (For interpretation of the references to color in this figure legend, the reader is referred to the web version of this article.)

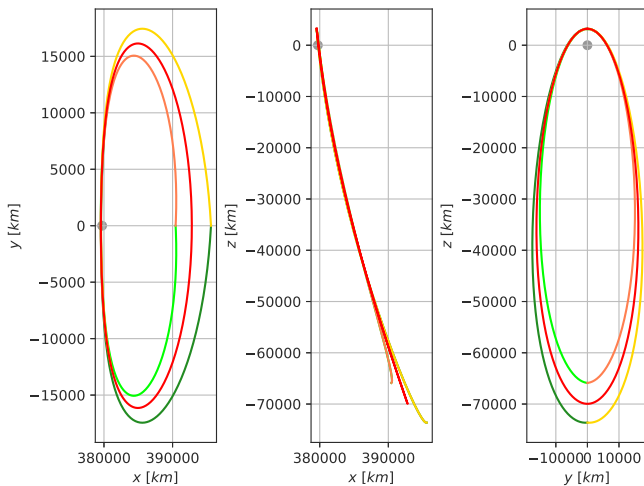


Fig. 14. Three-impulse phasing trajectories with $\Delta v_0 = 8$ m/s and highest TOF difference. UI to SE transfer in orange/light green, UE to SI in yellow/dark green — projections. (For interpretation of the references to color in this figure legend, the reader is referred to the web version of this article.)

TOF differences that might result if the orbit periodicity is not correctly taken into account. For any plane and crossing direction the maximum Δt across all considered departure and arrival positions θ_d, θ_a that satisfies $\Delta r < 200$ m is finally selected to assess the feasibility of the proposed solutions as possible phasing trajectories.

3.2.2. Low energy three impulses implementation

Deterministic maneuvers are thus introduced to ease departure and injection in the nominal NRHO while knowledge of the unstable and stable manifold directions at both maneuvering points is employed to determine the impulse direction. More in detail, transfer trajectories are constructed as follows. A discrete number of endpoint positions $\theta_d, \theta_a \in [0, 1]$ is firstly selected to define a great amount of possible departure and injection locations along the NRHO. Secondly, for each selected location the corresponding unstable and stable manifold directions are computed. A given maneuver amplitude Δv_0 is then imposed to obtain the initial and final states along the transfer path. Denoting with $\mathbf{x}_{d,0}, \mathbf{x}_{a,0}$ the orbit's states at θ_d, θ_a and with $\mathbf{v}_1^U, \mathbf{v}_2^S$ the unstable and

stable manifold directions at the same points, the transfer's initial and final states $\mathbf{x}_d^\pm, \mathbf{x}_a^\pm$ are thus computed as

$$\begin{aligned} \mathbf{x}_d^\pm &= \mathbf{x}_{d,0} \pm \Delta v_0 \cdot \frac{\begin{bmatrix} \mathbf{0}_{3 \times 1} \\ \mathbf{v}_{d,3:6}^U \end{bmatrix}}{\|\mathbf{v}_{d,3:6}^U\|} \\ \mathbf{x}_a^\pm &= \mathbf{x}_{a,0} \pm \Delta v_0 \cdot \frac{\begin{bmatrix} \mathbf{0}_{3 \times 1} \\ \mathbf{v}_{a,3:6}^S \end{bmatrix}}{\|\mathbf{v}_{a,3:6}^S\|} \end{aligned} \quad (20)$$

Note that Eq. (20) correspond to an impulsive maneuver applied at θ_d, θ_a with magnitude Δv_0 and direction given by the last three components of the unstable/stable eigenvector $\mathbf{v}_d^U, \mathbf{v}_a^S$ denoted with the subscript $3:6$. The \pm sign indicates the maneuver is applied along both the interior and exterior ways thus obtaining two possible departure and arrival states for the sought-after transfers. Once $\mathbf{x}_1^\pm, \mathbf{x}_2^\pm$ are known $\forall \theta_d, \theta_a$ the same states are propagated forward or backward in time until they intersect the $y = 0$ plane near the orbit's apselene ($v_y < 0$).

At this point, the connecting Δv_c is computed and the resultant total Δv is

$$\Delta v = 2 \cdot \Delta v_0 + \Delta v_c \quad (21)$$

4. Results

In this section the results obtained with the two phasing strategies are analyzed and their performance compared to highlight the complementarity of the proposed solutions.

4.1. Optimized two-impulses phasing

Numerical results are summarized in Fig. 5 where the best computed Δv are depicted against the departure orbit period T_d . As expected, the red curve corresponding to Δv exhibits an opposite trend to the blue one corresponding to T_{syn} and demonstrates that transfers become more costly for orbits farther from the target one. Another proof of this is shown in Fig. 6 where the ratio between the Jacobi constants (C_{jac}) of the departure and arrival orbits is represented. As much as the period differs from T_a , as much the required Δv increases given the increasing difference in orbital energy.

If less than 10 m/s are required departing from an orbit with $T_d = 6.77$ days, the transfer cost increases rapidly with T_d until it reaches a plateau $\Delta v \approx 80$ m/s for 10 days $< T_d < 12$ days. Moving further, departure orbits characterized by periods longer than 13 days require $\Delta v > 100$ m/s which exceed 350 m/s for L_2 Halos very close to the libration point.

As a consequence, EML-2 Halos with periods 8 days $< T_d < 9$ days are finally identified as feasible intermediate orbits since they guarantee a good compromise between $\Delta v \in [45, 70]$ m/s and maximum WT, being the last directly correlated with the synodic period $T_{syn} \in [24, 36]$ days.

An example transfer departing from an L_2 Halo with $T_d = 8.21$ days is depicted in Figs. 7 and 8 in a synodic frame centered on the Earth–Moon barycenter. The transfer requires a total $\Delta v = 51.97$ m/s and a $TOF = 4.67$ days while the Halo-NRHO synodic period is equal to $T_{syn} = 32.70$ days.

Indeed the selected Halo has $T_d = 8.5$ days, $R_p = 9718.523$ km, Jacobi constant $C_{jac} = 3.034$ and stability indexes $s_1 = -1.604$ and $s_2 = 0.175$. The last indicates that the parking orbit is less stable than the target one (see Table 1), but this could be a desirable property since the spacecraft is required to stay on this orbit only for a limited amount of time and the depart towards the target one. Therefore, the sensitivity analysis is performed on this orbit. The obtained results are visualized in Fig. 9.

It is clear that the transfer can be performed with and maximum expenditure that is less than 80 m/s and larger than 58 m/s. With a total transfer time that stays between 1 and 4 NRHO orbital periods.

Table 2
Total Δv , TOF and TOF difference w.r.t. Δv_0 for three-impulse phasing trajectories.

Δv_0 [m/s]	UI to SE transfers				UE to SI transfers			
	Δv [m/s]	TOF [days]	ΔTOF [H]	$\Delta\theta$ [°]	Δv [m/s]	TOF [days]	ΔTOF [H]	$\Delta\theta$ [°]
1.0	4.874379	6.918131	−1.698597	−0.010784	4.878503	7.059597	1.696592	0.010784
2.0	9.651215	6.814502	−3.398221	−0.021576	9.838622	7.162984	3.390394	0.021576
4.0	19.273416	6.672873	−6.797320	−0.043158	19.685066	7.303630	6.765883	0.043158
8.0	37.492437	6.325116	−13.568514	−0.086151	39.658996	7.614753	13.445357	0.086151
16.0	72.816148	5.741168	−26.795792	−0.170135	80.222142	8.218163	26.352229	0.170138

4.2. Low energy three impulses transfers

The different manifold intersection on different Poincare maps are studied and reported in Figs. 10 to 12. Thanks to the geometry and the relative distance between the stable and unstable manifolds (< 200 m) the Poincare map $y = 0$ is selected for transfer design. Different Δv_0 are then applied to inject the spacecraft in the diverging manifold (and by symmetry to re-enter the NRHO) and the total Δv , which includes the discontinuity near the orbit's apselene, is computed together with the recover in time.

The Δt in Table 2 can be easily converted in $\Delta\theta$ through Eq. (22)

$$\Delta\theta = \frac{\Delta TOF}{T_{NRHO}} \quad (22)$$

Unstable and stable manifold directions for the nominal NRHO might be effectively exploited to design three-impulses phasing trajectories that reduce the time gap between the chaser vehicle and the target station while flying along the same orbit. Transfers with total TOF longer than the baseline NRHO (UE to SI type, $\Delta t > 0$) are suitable for visiting vehicles initially ahead of the station while trajectories with shorter TOF (UI to SE type, $\Delta t < 0$) must be exploited by spacecraft initially behind it. This study limits the TOF along the nominal path to about one orbit period and the initial and final impulses to $\Delta v_0 \leq 16$ m/s. These assumptions allow constructing UI to SE type transfers characterized by a maximum TOF difference of ~ 26.80 h and total $\Delta v = 72.82$ m/s. At the same time, UE to SI type transfers might be designed to lose up to 26.35 h with a total maneuvering cost of $\Delta v = 80.22$ m/s. An example of phasing trajectory obtained with this method is shown in Figs. 13 and 14.

5. Conclusions

Different phasing strategies for target resupply vehicles are analyzed in this paper. Optimal two-impulses transfers targeting the station's baseline NRHO from several members of the EML-2 Halo family are computed. To limit the total transfer time, the Halo-NRHO synodic period T_{syn} is introduced here to estimate an upper bound on the WT needed for the chaser to attain the most favorable relative configuration in the worst-case scenario. It is finally demonstrated that viable transfer options exist with $\Delta v < 80$ m/s and total TOF (including WT) under 40 days.

A different phasing strategy is then proposed assuming the chaser vehicle is directly injected in the final NRHO at the end of the translunar transfer phase. Poincare maps are employed to identify unstable/stable manifold intersections in search of low-energy phasing trajectories that leave the reference orbit along the unstable branch before re-entering it via the stable one. If several candidate intersections are found, spacecraft flying along the corresponding trajectories would gain a negligible phase difference with respect to the lunar station given that the invariant manifolds remain near the reference NRHO for propagation times longer than 5 orbit periods. Deterministic maneuvers performed at both transfers' endpoints are thus introduced to excite the unstable/stable manifold directions and accelerate orbit's divergence from the nominal path. Perturbed states are then propagated until their paths cross the $y = 0$ plane where diverging/converging

branches intersections are sought. This procedure is successfully employed to determine three-impulses phasing trajectories with maximum TOF differences in the order of one day for a total $\Delta v < 80$ m/s.

To conclude, both strategies are applicable to perform phasing with an L_2 NRHO, with the two-impulses strategy suitable for smaller phase differences and the three impulses strategy indicated for larger differences since it allows further energy savings in these particular conditions.

Declaration of competing interest

The authors declare that they have no known competing financial interests or personal relationships that could have appeared to influence the work reported in this paper.

References

- [1] NASA, The Artemis Plan - NASA's Lunar Exploration Program Overview, Tech. Rep., 2020, URL https://www.nasa.gov/sites/default/files/atoms/files/artemis_plan-20200921.pdf.
- [2] R. Whitley, R. Martinez, Options for staging orbits in cislunar space, in: 2016 IEEE Aerospace Conference, 2016, pp. 1–9, <http://dx.doi.org/10.1109/AERO.2016.7500635>.
- [3] R.J. Whitley, D.C. Davis, L.M. Burke, B.P. McCarthy, J. Power, M.L. McGuire, K.C. Howell, Earth-moon near rectilinear halo and butterfly orbits for lunar surface exploration, in: AAS/AIAA Astrodynamics Specialist Conference, Snowbird, Utah, USA, 2018, p. 20.
- [4] J. Williams, D.E. Lee, R.J. Whitley, K.A. Bokelmann, D.C. Davis, C.F. Berry, Targeting cislunar near rectilinear halo orbits for human space exploration, in: 27th AAS/AIAA Space Flight Mechanics Meeting, San Antonio, TX, USA, 2017, p. 20.
- [5] D.E. Lee, White Paper: Gateway Destination Orbit Model: A Continuous 15 Year NRHO Reference Trajectory, Technical Report JSC-E-DAA-TN72594, National Aeronautics and Space Administration, NASA Johnson Space Center, Houston, TX, United States, 2019, p. 6, URL <https://ntrs.nasa.gov/api/citations/20190030294/downloads/20190030294.pdf>.
- [6] L. Hiday, K. Howell, Impulsive time-free transfers between halo orbits, in: Astrodynamics Conference, American Institute of Aeronautics and Astronautics, Hilton Head Island, SC, U.S.A., 1992, <http://dx.doi.org/10.2514/6.1992-4580>.
- [7] K. Howell, L. Hiday-Johnston, Time-free transfers between libration-point orbits in the elliptic restricted problem, Acta Astronaut. 32 (4) (1994) 245–254, [http://dx.doi.org/10.1016/0094-5765\(94\)90077-9](http://dx.doi.org/10.1016/0094-5765(94)90077-9).
- [8] K.E. Davis, R.L. Anderson, D.J. Scheeres, G.H. Born, Locally optimal transfers between libration point orbits using invariant manifolds, in: Advances in the Astronautical Sciences, Vol. 135, Pittsburgh, Pennsylvania, 2009.
- [9] K.E. Davis, R.L. Anderson, D.J. Scheeres, G.H. Born, Optimal transfers between unstable periodic orbits using invariant manifolds, Celestial Mech. Dynam. Astronom. 109 (3) (2011) 241–264, <http://dx.doi.org/10.1007/s10569-010-9327-x>.
- [10] K.A. Bokelmann, R.P. Russell, Optimization of impulsive Europa capture trajectories using primer vector theory, J. Astronaut. Sci. 67 (2) (2020) 485–510, <http://dx.doi.org/10.1007/s40295-018-00146-z>.
- [11] N.L.O. Parrish, Low Thrust Trajectory Optimization in Cislunar and Translunar Space (Ph.D. thesis), University of Colorado at Boulder, 2018.
- [12] E. Taheri, V. Arya, J.L. Junkins, Acceleration-based indirect method for continuous and impulsive trajectory design.
- [13] J. Zhou, J. Hu, Y. Bai, B. Zhang, Optimal impulsive time-fixed transfers around the libration points of the restricted three-body problem, Astrophys. Space Sci. 365 (5) (2020) 1–18.
- [14] G. Burchioni, M. Innocenti, Design of the phasing trajectory from a low Lunar orbit to near rectilinear halo orbit, in: AIAA/AAS Astrodynamics Specialist Conference, 2020, p. 20.
- [15] K.E. Davis, R.L. Anderson, G.H. Born, D.J. Scheeres, Connecting libration point orbits of different energies using invariant manifolds, in: Advances in the Astronautical Sciences, Vol. 134, Savannah, Georgia, 2009.

- [16] W.S. Koon, M.W. Lo, J.E. Marsden, S.D. Ross, Dynamical systems, the three-body problem and space mission design, 2011, URL http://www.cds.caltech.edu/~koon/book/KoLoMaRo_DMissionBook_2011-04-25.pdf.
- [17] D.C. Davis, E.M. Zimovan-Spreen, R.J. Power, K.C. Howell, Cubesat deployment from a near rectilinear halo orbit, in: AIAA SCITECH 2022 Forum, 2022, p. 1777.
- [18] E.M. Zimovan, K.C. Howell, D.C. Davis, Near rectilinear halo orbits and their application in Cis-Lunar space, in: 3rd International Academy of Astronautics Conference on Dynamics and Control of Space Systems, Moscow, Russia, 2017, p. 20.
- [19] E. Blazquez, SEMpy: a python open-source toolbox for non-Keplerian astrodynamics, in: International Conference on Astrodynamics Tools and Techniques (ICATT), 2021, Virtual.
- [20] NASA, General mission analysis tool (GMAT). URL <http://gmtcentral.org>.
- [21] CNES, CelestLab. URL <http://atoms.scilab.org/toolboxes/celestlab>.
- [22] CS GROUP, Orekit. URL <http://www.orekit.org/>.
- [23] E. Blazquez, L. Beauregard, S. Lizy-Destrez, F. Ankersen, F. Capolupo, Rendezvous design in a cislunar near rectilinear Halo orbit, *Aeronaut. J.* 124 (1276) (2020) 821–837, <http://dx.doi.org/10.1017/aer.2019.126>.
- [24] S. Lizy-Destrez, L. Beauregard, E. Blazquez, A. Campolo, S. Manglativi, V. Quet, Rendezvous strategies in the vicinity of earth-moon Lagrangian points, *Front. Astron. Space Sci.* 5 (2019) 45, <http://dx.doi.org/10.3389/fspas.2018.00045>.
- [25] T. Pavlak, Trajectory Design and Orbit Maintenance Strategies in Multi-Body Dynamical Regimes (Ph.D. thesis), Purdue University, West Lafayette, Indiana, 2013, URL https://engineering.purdue.edu/people/kathleen.howell.1/Publications/Dissertations/2013_Pavlak.pdf.
- [26] D.L. Richardson, Analytic construction of periodic orbits about the collinear points, *Celestial Mech.* 22 (3) (1980) 241–253, <http://dx.doi.org/10.1007/BF01229511>.